

## Abdellah Kharicha<sup>1</sup>

Department of Metallurgy,  
University of Leoben,  
Franz Josef-Strasse 18,  
Leoben 8700, Austria  
e-mail: abdellah.kharicha@unileoben.ac.at

## Jan Bohacek

Department of Metallurgy,  
University of Leoben,  
Franz Josef-Strasse 18,  
Leoben 8700, Austria  
e-mail: jan.bohacek@unileoben.ac.at

## Andreas Ludwig

Professor  
Department of Metallurgy,  
University of Leoben,  
Franz Josef-Strasse 18,  
Leoben 8700, Austria  
e-mail: andreas.ludwig@unileoben.ac.at

## Menghuai Wu

Laboratory for Advanced Simulation  
of Solidification and Melting  
Department of Metallurgy,  
University of Leoben,  
Franz Josef-Strasse 18,  
Leoben 8700, Austria  
e-mail: menghuai.wu@unileoben.ac.at

# Modified Shallow Water Equations With Application for Horizontal Centrifugal Casting of Rolls

*A numerical model based on the shallow water equations (SWE) was proposed to simulate the two-dimensional (2D) average flow dynamics of the liquid metal spreading inside a horizontally rotating mold. The SWE were modified to account for the forces, such as the centrifugal force, Coriolis force, shear force with the mold wall, and gravity. In addition, inherent vibrations caused by a poor roundness of the mold and the mold deformation due to temperature gradients were applied explicitly by perturbing the gravity and the axis bending, respectively. Several cases were studied with the following initial conditions: a constant average height of the liquid metal (5, 10, 20, 30, and 40 mm) patched as a flat or a perturbed surface. The angular frequency  $\Omega$  of the mold ( $\varnothing 1150\text{--}3200$ ) was 71.2 (or 30) rad/s. Results showed various wave patterns propagating on the free surface. In early stages, a single longitudinal wave moved around the circumference. As the time proceeded, it slowly diminished and waves traveled mainly in the axial direction. It was found that the mean amplitude of the oscillations grows with the increasing liquid height. [DOI: 10.1115/1.4030760]*

## 1 Introduction

The horizontal centrifugal casting (HSC) is a casting process that has several advantages over the traditional gravity casting processes. The schematic of the HSC process is shown in Fig. 1. Centrifugally cast products have a high degree of metallurgical purity and homogeneous microstructure. A significant gain is observed for the rupture strength, the rupture strain, the fatigue resistance, and the Young's modulus as discussed, e.g., by Shailesh et al. [1]. These properties naturally depend on the centrifugal force and thus, the best mechanical properties can be found at the largest distance from the axis of rotation. However, a proper selection of the angular frequency  $\Omega$  has to be done in order to prevent the so-called "metal raining," i.e., metal droplets falling down from the upper part of the mold due to a too weak centrifugal acceleration. In the same time, excessive speeds can lead to the appearance of longitudinal cracks caused by the hoop stress in the initially solidified layer. From empirical knowledge, other parameters have an important influence on the casting products, it includes the pouring temperature, the pouring rate, the mold coating, etc. Recently, Chirita et al. [2] identified natural or forced vibrations as possible additional factors to be taken into account. Although mechanisms are not yet clear, the vibrations influence the solidification structure and the level of porosity. Earlier, Chirita et al. [3] observed a transition from the lamellar to the fibrous morphology with the increase of the vibration amplitude. An

influence on the eutectic fraction was also observed. If the acceleration related to the vibration reaches a critical magnitude, the grains tend to coarsen. It is generally assumed that during the centrifugal casting, the melt first solidifies on the mold wall, then due to the turbulent flow, fragments are moved back into the melt and stand as a new nucleation sites as described by Chang et al. [4]. It is believed that vibrations can significantly enhance this grain refining process.

In most of the scientific papers, numerical studies of the centrifugal casting usually rely on commercial CFD packages. Certainly, the most common approach for solving the free-surface flows is

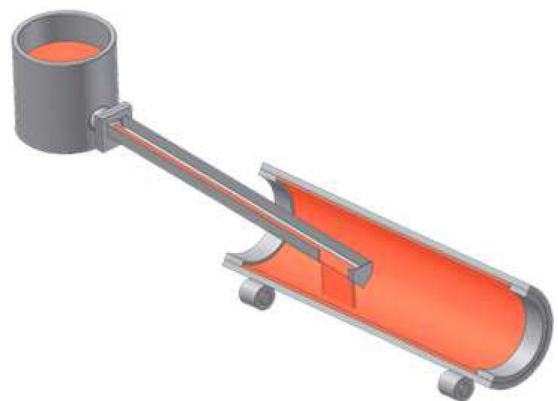


**Fig. 1** A schematic of the horizontal centrifugal casting of the outer shell of a work roll

<sup>1</sup>Corresponding author.

Contributed by the Fluids Engineering Division of ASME for publication in the JOURNAL OF FLUIDS ENGINEERING. Manuscript received February 24, 2014; final manuscript received May 28, 2015; published online July 21, 2015. Assoc. Editor: Samuel Paolucci.

the volume of fluid (VOF) method by Hirt and Nichols [5], which is very robust and applicable to various free-surface flows. Unfortunately, to accurately track the interface a very fine grid is usually required and moreover, one has to solve the flow also in the ambient phase, which is rather redundant in the case of the HSC. In the paper by Keerthiprasad et al. [6], an effort for a comprehensive description of the flow dynamics of the melt inside the horizontally rotating mold including the mold filling was done using the VOF model (STAR-CD). Two phases were considered, the liquid metal and the surrounding air. The time step was notably large ( $\sim 0.01$  s), which implies a very rough calculation. Nevertheless, the results were found to be in quite good agreement with experimental data. The VOF method was also used in work done by Zagorski and Sleziona [7] to study the initial stage of mold filling during the vertical centrifugal casting of metal matrix composite reinforced with SiC. Additionally, a discrete phase model was used to track SiC particles. The problem was solved as 2D axisymmetric with swirl component of velocity and all calculations were terminated at 1 s of real-time. At a sufficiently high rotating speed of the mold, the liquid metal rotates with the mold. Therefore, it is convenient to solve the task in the rotating frame of reference, i.e., to take into account fictitious forces such as the centrifugal and Coriolis force. This approach naturally allows using much larger time steps resulting in a significant speed-up of calculations. Recently, this solution strategy was adopted by Kaschnitz [8], where the horizontal centrifugal pipe casting process was solved using FLOW-3D. Although the flow algorithm does not consider the flow within the ambient air, the normal computation still took around 20 days for a relatively rough mesh. To overcome mesh-dependent results, the numerical model was tuned by adjusting the viscosity, turbulent properties, and comparing numerical results with the experiment. Next, the effect of fictitious forces on the mold filling during the vertical centrifugal casting was investigated again by using the VOF model [9]. They found that the Coriolis force can cause remarkable variations in the flow patterns in the casting-part-cavities of a large horizontal-section area and directly connected to the sprue. Another recent study of the mold filling was performed by Xu et al. [10], in which the effect of the static and moveable filling on the temperature distribution during the HSC of a work roll was studied. The second naturally produces a more uniform temperature distribution, which could lead to the elimination of the so-called sapling defects. The flow algorithm is based on the VOF free-surface tracking method. Since simulations were focused on the filling ( $\sim 30$  s), the full HSC process ( $\sim 35$  mins) was not of concern and the algorithm performance or computational times were not discussed. Fjeld and Ludwig [11] performed a numerical study of the casting of a work roll core. The popular VOF method was employed to track the interface between the liquid metal and air. The remelting of the outer shell was mainly investigated (more details related to simulations of multiphase phenomena are clearly discussed in the work by Ludwig et al. [12]).

The aim of the present model is a development of an effective flow algorithm for tracking the free surface of a thin liquid layer inside a horizontally rotating cylindrical mold representing the outer shell of a work roll. Numerical simulations are focused on the investigation of wave patterns appearing on the free surface due to the interaction of the inertia forces including fictitious forces and other body forces, such as the gravity and forces resulting from mold vibrations. In the future, the current numerical model will be extended to account for the solidification and the heat transfer including the radiation inside the mold. From a long-term perspective, we target on the simulation of the full HSC process, i.e., the casting of both the outer (the high-speed steel) and the intermediate (the gray cast iron) layer. The HSC process is finished after approximately 35 mins when the mold is turned in the vertical position and the gravity casting of the core takes place. By comparing the HSC time ( $\sim 35$  mins) with relatively high velocities of the liquid metal ( $\sim 1$  m/s), we can conclude that the algorithm has to be extremely fast and efficient.

## 2 Numerical Model

The present model is based on the SWE. The SWE are widely used for modeling purposes in oceanography and also meteorology. Its original form can be found in the book by Leveque [13] and are used for a mathematical description of the so-called gravity waves. The SWE can be generalized to account for various physical phenomena, such as the Coriolis force, flow over variable topography, and bed shear stress, which are discussed, e.g., in Dellar and Salmon [14] and Hirt and Richardson [15]. The SWE usually refer to the modeling of the so-called gravity waves. In the literature, the SWE can be found derived in the Cartesian coordinate system as well as in the spherical coordinate system [16], but no application of the SWE could be found for the cylindrical geometry. Note that by using the SWE, the momentum equation in the direction perpendicular to the underlying topography is always omitted. In other words, under certain conditions a three-dimensional (3D) problem can be transformed into a 2D problem, which can still resolve the height in the vertical (or radial) direction.

Here, we present a shallow water model for modeling the average flow dynamics of the thin liquid layer inside a horizontally rotating mold (see Fig. 1). The SWE were derived in the rotating frame of reference, i.e., fictitious forces were included in the model. The SWE were further modified in order to account for the variable topography representing the liquid/solid interface. The solidification and heat transfer are, however, out of the scope of this paper. A general situation is depicted in Fig. 2, in which the parabolic velocity profile indicates the assumption of the fully developed laminar flow.

Next, we assume a no-slip boundary condition (BC) with the underlying topography. On the free surface, the friction with air and surface tension effects is neglected. The liquid height  $h$  is small compared to the internal radius  $R$  of the mold; therefore, the

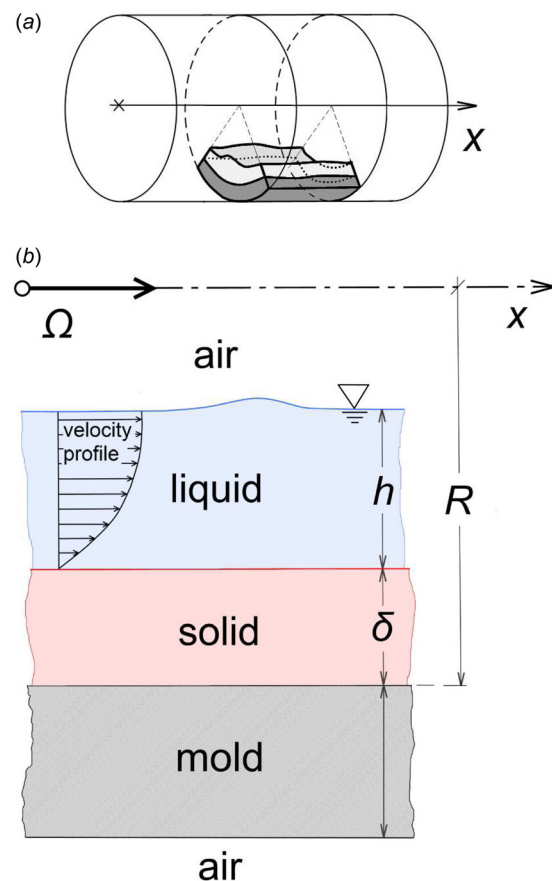


Fig. 2 A schematic of a part of the HSC section

problem can be still solved in the Cartesian coordinates  $(x, y)$  representing the axial and tangential direction, respectively. Perhaps, the most important assumption applies to neglecting all vertical (or radial) components in momentum equations except the gradients of the hydrostatic pressure. In the shallow water terminology, this is often called the condition of the hydrostatic balance discussed by Audusse et al. [17].

The continuity equation takes the form

$$\frac{\partial(h\rho)}{\partial t} + \nabla \cdot (h\rho\bar{\mathbf{u}}) = 0 \quad (1)$$

where the liquid density  $\rho$  is a constant in the model ( $\sim 6800 \text{ kg/m}^3$ ), and  $\bar{\mathbf{u}}$  is the mass flow averaged velocity of the liquid. The momentum equations can be expressed in the vectorial form as follows:

$$\frac{\partial(h\rho\bar{\mathbf{u}})}{\partial t} + \bar{\mathbf{u}} \cdot (\nabla(h\rho\bar{\mathbf{u}})) + \mathbf{F}_c + \mathbf{F}_C = -h\nabla p + h\mu\nabla^2\bar{\mathbf{u}} + \mathbf{F}_\tau + \mathbf{F}_g \quad (2)$$

where the terms on the left-hand side represent the inertia forces including the fictitious forces. The centrifugal force  $\mathbf{F}_c$  is derived from the centrifugal acceleration  $\mathbf{a}_c$  given by

$$\mathbf{a}_c = \Omega \times (\Omega \times \mathbf{r}) \quad (3)$$

where  $\mathbf{r}$  is the position vector. The centrifugal force  $\mathbf{F}_c$  always pushes the liquid outward. For a perfectly cylindrical mold, the only nonzero component of the centrifugal acceleration  $\mathbf{a}_c$  is the radial component  $a_{cr}$ . The radial component  $a_{cr}$  cannot be, however, applied directly in Eq. (2). It has to be first expressed as an equivalent hydrostatic pressure. Then, the integral of the gradient of this hydrostatic pressure over the liquid height  $h$  gives the axial and tangential components of the centrifugal force  $\mathbf{F}_c$  used in Eq. (2). The same procedure is applied on all other body forces having a nonzero radial component. A detailed derivation of the centrifugal force  $\mathbf{F}_c$  can be found in Appendix B. The Coriolis force  $\mathbf{F}_C$  is derived from the Coriolis acceleration  $\mathbf{a}_C$ , which depends on the relative velocity  $\mathbf{u}$  and is given by

$$\mathbf{a}_C = 2\Omega \times \mathbf{u} \quad (4)$$

Unlike the centrifugal force  $\mathbf{F}_c$ , the Coriolis force  $\mathbf{F}_C$  either pushes the liquid inward or outward depending on the orientation of the relative velocity  $\mathbf{u}$ . Note that this is only true for a perfectly cylindrical mold and the angular frequency  $\Omega$  parallel to the mold axis. For more details, see Appendix C. On the right-hand side of Eq. (2), the first two terms represent the force resulting from the static pressure difference and the viscous force derived from the shear stresses in the plane  $(x, y)$ , respectively. Note that the viscous force does not account for the shear force with the mold due

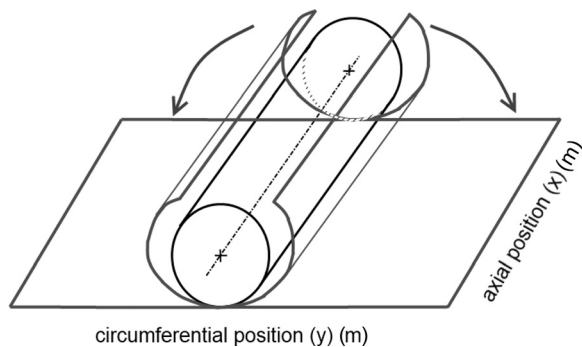


Fig. 3 A schematic of the computational domain created by unfolding the internal cylindrical surface of the mold into the plane  $(x, y)$

to the no-slip BC imposed. The bed shear force with the mold depends on the parabolic velocity profile and is applied separately denoted by  $\mathbf{F}_\tau$  (Appendix F). The last term in Eq. (2) refers to the gravity force  $\mathbf{F}_g$ , which in the rotating frame of reference is a vector rotating in the opposite direction of the rotating mold  $(-\Omega)$ . The final formulas for  $\mathbf{F}_g$  used in Eq. (2) are discussed in detail in Appendix D. In addition to the free-surface BCs and the BCs on the liquid/solid interface both described earlier, we apply a reflective wall at the mold extremities. In Fig. 3, this corresponds to the boundaries parallel to the circumferential position. Finally, periodic boundary conditions are used at the boundaries denoting the axial position.

### 3 Vibrations and Mold Deformation

The HSC of work rolls is always accompanied by inherited vibrations induced by a static imbalance of the mold, a poor circularity of rolling tracks or carrying rollers, and also by an axial deformation of the mold due to thermal expansion effects (Martinez et al. [18]). Fundamental principles about vibrations of cylindrical shells are stated in Love's [19] and Donnell's [20] theory both based on the thin shell equations. Each object with a certain mass and a stiffness including the cylindrical mold prefers to oscillate at its natural frequencies  $f_n$ . Each of these frequencies is associated with a mode shape and a damping coefficient. The natural frequency  $f_n$  is a function of the mass and the stiffness, which depends on the dimensions of the object and the Young's modulus. For geometrically simple objects, such as a beam or a cantilever, a unique mode shape  $m$  exists for each natural frequency  $f_n$ . This is, however, not true for cylindrical shells, for which a unique pair of mode shapes  $m$  and  $n$  exists for each natural frequency  $f_n$  as discussed in Ref. [21]. The mode shape  $m$  refers to a number of axial half waves, whereas the mode shape  $n$  applies to a number of circumferential full waves (Fig. 4). For a static cylinder, each mode shape is represented by a standing

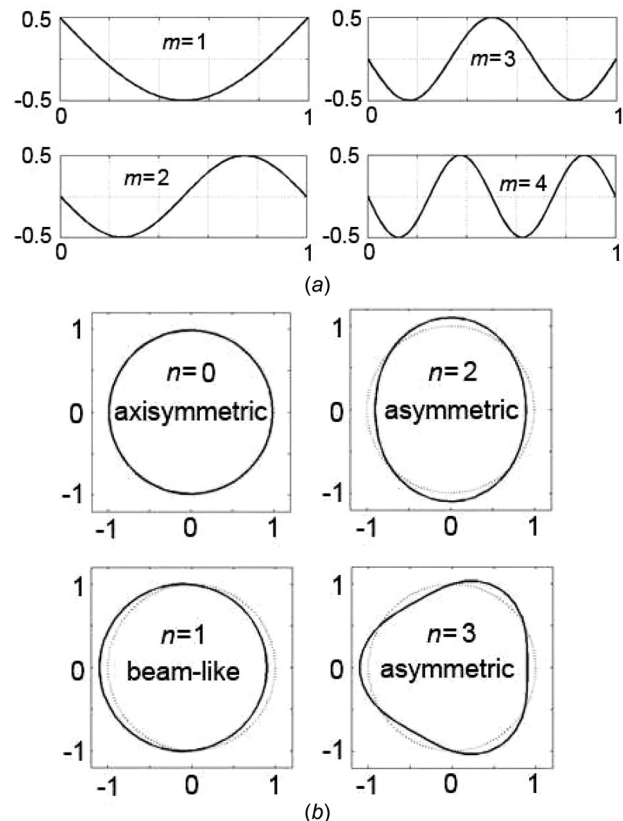
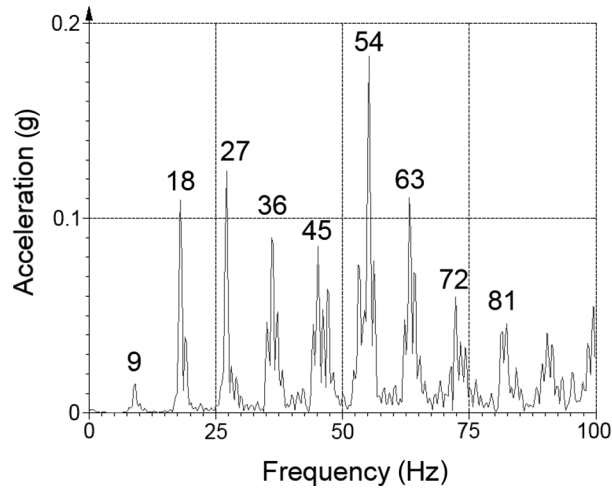


Fig. 4 Mode shapes of a vibrating cylindrical shell: (a) axial mode shapes and (b) circumferential mode shapes



**Fig. 5 A frequency spectrum of the horizontally accelerating carrying roller perpendicular to the mold axis**

wave oscillating around its nodes. However, in rotating cylindrical shells mode shapes travel and lag behind the rotation of the cylinder, which is called the Bryan effect [22].

Experimentally, a link between mode shapes and the vibration recorded during the real casting was found with the help of a frequency spectrum of the acceleration of the arbitrary carrying roller measured in a horizontal plane and perpendicular to the mold axis. An example of the experimental data is shown in Fig. 5 for a particular casting with the angular frequency  $\Omega$  of the rotating mold corresponding to 9 Hz. The obvious harmonics are integer multiples of the angular frequency  $\Omega$ , which implies a qualitative connection with the mode shapes. Higher harmonics correspond to more complicated mode shapes.

The present paper aims to study a response of the free surface to a specific vibration mode. The study is simplified by only considering one pair of the axial and the circumferential mode shape. We introduce the bending of the axis to reproduce the axial mode shape ( $m=1$ ) (see Appendix A). The presence of the axis bending modifies all body forces mentioned in Eq. (2) (a derivation of these forces is detailed in Appendices B, C, and D). The circumferential mode shape ( $n=2$ ) is applied directly by perturbing the gravity with details given in Appendix E.

#### 4 Results and Discussion

All simulations were run with constant physical properties of the liquid metal ( $\rho = 6800 \text{ kg/m}^3$  and  $\mu = 0.006 \text{ kg/m s}$ ). The mold is 3.2 m long and the inner mold radius is  $R = 0.372 \text{ m}$ . Two

**Table 1 List of model settings for the cases N1–N12**

	$\Omega$ (rad/s)	$h$ (mm)	Vibrations	Axis bending	Initial perturbation
N1	71.2	5	Yes	No	Yes
N2		10			
N3		20			
N4		30			
N5		40			
N6		5			No
N7		10			
N8	30	20			
N9					Yes
N10			No		No
N11				Yes	
N12			Yes		

different angular frequencies  $\Omega$  were considered: 30 rad/s and 71.2 rad/s. Several liquid layer heights  $h$  were simulated (5, 10, 20, 30, and 40 mm). An initial distribution of the liquid height  $h$  was imposed. Two distinct initial liquid height distributions were considered, either a flat surface with a constant liquid height  $h$  or a surface perturbed by the following function:

$$h = \bar{h} \left[ \sin(p(x-q)^2) + \sin(r(y-s)^2) \right] \quad (5)$$

where  $\bar{h}$  is the mean liquid height. Constants  $p$ ,  $q$ ,  $r$ , and  $s$  are 10, 0.4, 12, and 0.3, respectively. The function given by Eq. (5) was chosen in order to perturb the free surface with different wavelengths in both directions,  $x$  and  $y$ . Several cases (N1–N12) corresponding to different model settings (Table 1) were calculated. The time step was held constant ( $\Delta t = 0.001 \text{ s}$ ) so that the local Courant number was always smaller than 0.1 for both angular frequencies  $\Omega$  used. Second-order schemes were used for the space and time discretization.

Examples of an instantaneous shape of the free surface are shown in the  $xy$ -plane representing the axial and tangential direction in Figs. 6 and 7. At early stage of the simulation, a single wave travels along the cylinder circumference. In the case without the axis bending, the longitudinal wave does not vary along the axial direction (Fig. 6(a)). On the contrary, the longitudinal wave immediately responds to the nonzero axis bending and varies along the axial direction (Fig. 6(b)). In a fully developed flow regime, the longitudinal wave is no longer visible and a complex wave pattern is formed (Fig. 7). Without the axis bending, the pattern of the free surface resembles annular waves (Fig. 7(a)), whereas with the axis bending the pattern is more chaotic (Fig. 7(b)).

The results were compared by means of the mean amplitude defined as

$$\bar{A}_n = \frac{h_{\max} - h_{\min}}{2} \quad (6)$$

where  $h_{\max}$  and  $h_{\min}$  are the maximum and the minimum liquid height found in the entire computational domain. Such an

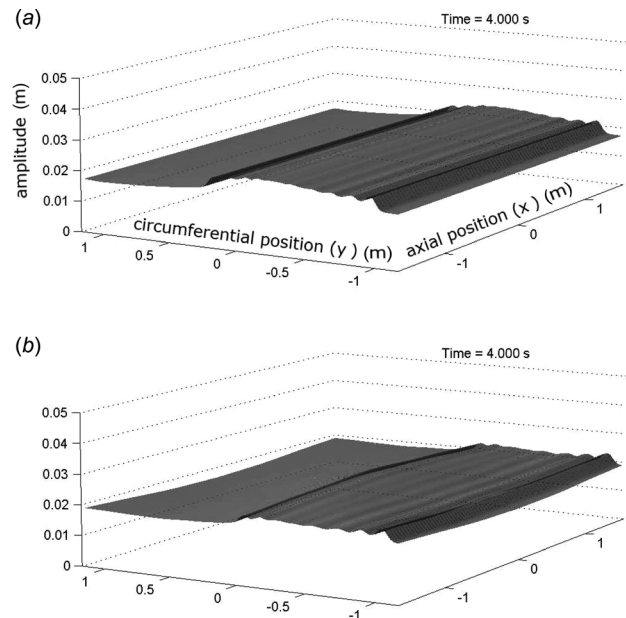


**Fig. 6 An instantaneous shape of the free surface at 4 s for N8 and N12, respectively. (a) A constant liquid height  $h$  along the axial direction. (b) An influence of the axis bending on the longitudinal wave formed during the early stage of the simulation.**

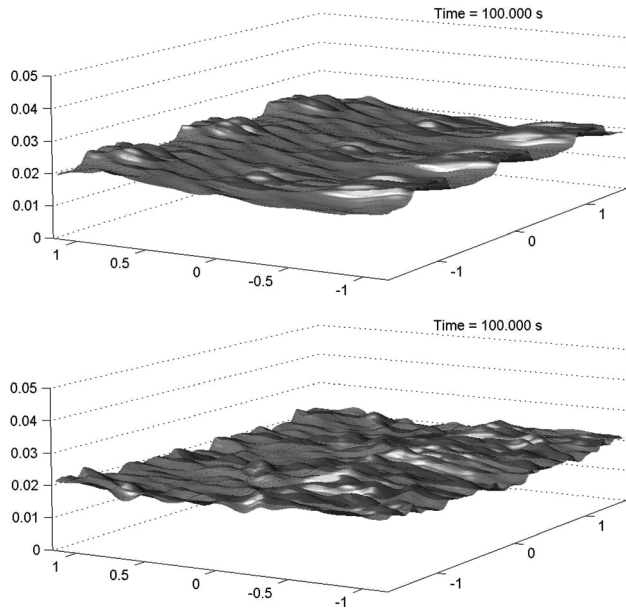


**Fig. 7** A fully developed pattern at 100s for *N8* and *N12*, respectively. (a) A pattern resembling annular waves and (b) A pattern disrupted by the presence of the axis bending.

amplitude, however, shows strong fluctuations (a thickly fluctuating signal in Fig. 8); therefore, the resulting data were convolved with the Gaussian kernel (a line with a circle marker in Fig. 8) to obtain the main evolution. The evolution of the mean amplitudes is shown in Fig. 8 for the angular frequency  $\Omega$  of 71.2 rad/s and in Fig. 9 for  $\Omega = 30$  rad/s. Several general features can be drawn from the results:

- (1) Mean amplitudes never drop to zero within the calculated time range ( $\approx 180$  s). Certain waves survive even for small liquid heights.
- (2) A single longitudinal wave is formed in early stages due to the gravity and the inertia interaction no matter whether the free surface was initially perturbed or not. As the velocity field develops, the longitudinal wave diminishes within an apparent relaxation time ranging from 20 s to 40 s.
- (3) The higher the liquid height  $h$ , the higher is the mean amplitude of the oscillations.

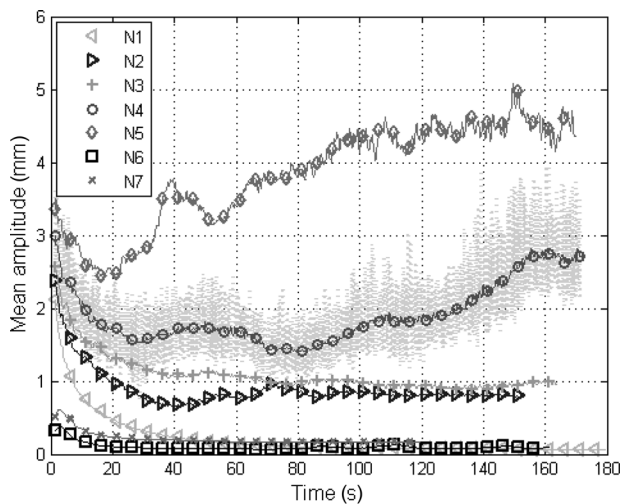


**Fig. 8** An evolution of the mean amplitude of the free surface for  $\Omega = 71.2$  rad/s

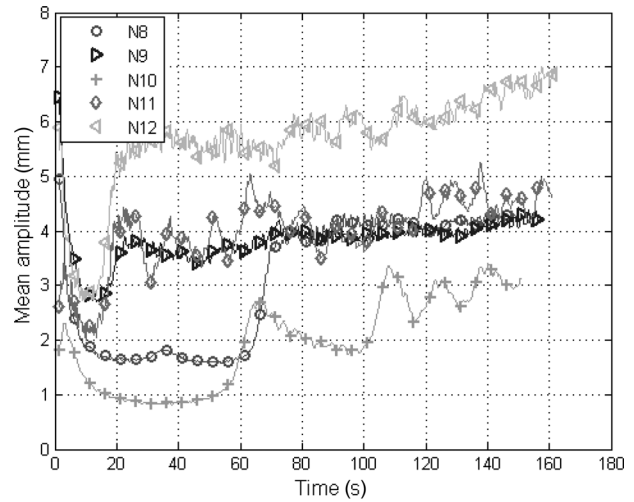


**Fig. 9** An evolution of the mean amplitude of the free surface for  $\Omega = 30$  rad/s

- (4) In all final states, waves are traveling mainly in the axial direction. This transfer of momentum from the circumferential and radial directions (gravity and vibrations) to the axial direction is due to the rotational nature of the Coriolis force.

Almost no influence of the initial perturbation on the final state can be observed between the cases *N1* and *N6* (Fig. 8). Without the perturbation case, *N7* converges toward a relatively quiet state, with the perturbation the same case converges toward a state where the oscillations are four times larger. At lower rotation speed, a transition between a calm and dynamic state occurs after 60 s real-time. In Fig. 9, notice the relatively low amplitude region from 20 s to 60 s with a sudden transition to instability at 60 s. *N10* with no vibrations involved is significantly different compared to *N8*. By comparing case *N10* with cases *N8* and *N9*, it can be stated that vibrations amplify and stabilize the amplitude of oscillations of the interface. The same behavior is found for the cases *N11* and *N12* both with the axis bending and without and with the vibrations, respectively. The origin of the stabilizing effects of the perturbations is not yet clear. From Fig. 9, it is also evident that the axis bending significantly reduces the time necessary for the transition to instability.

A verification of the SWE model was done using the hydrostatic free-surface model discussed in detail, e.g., in the paper by Casulli [23]. The hydrostatic free-surface model is an intermediate step between the SWE model and a fully nonhydrostatic free-surface model such as the VOF and the level set method [24]. Unlike these generally expensive nonhydrostatic free-surface models, the hydrostatic free-surface model neglects effects of the

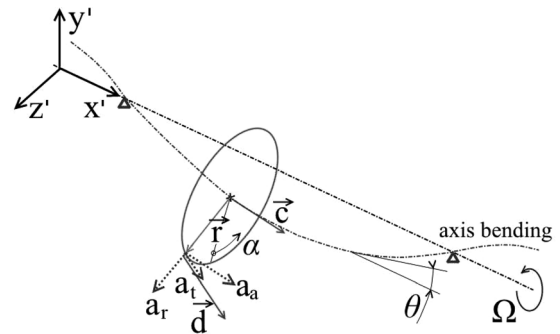


**Fig. 10** A verification of the SWE model; a comparison with the hydrostatic free-surface model by Casulli [23]

nonhydrostatic pressure. However, the efficiency of the algorithm is greatly improved. On the other hand, when compared with the SWE model, the complexity of the hydrostatic free-surface model is increased by resolving horizontal velocity components along the height of the liquid layer and reconstructing the vertical velocity components using the continuity equation. Here, the verification was realized by comparing waves propagating after a collapse of the liquid parabola. The initial liquid height was defined by the following formula:

$$h_0(x, 0) = 0.03 + \max(0, 0.03 - 5(x - 0.5)^2) \quad (7)$$

Other simulation settings were identical to those used in the aforementioned simulations with the angular frequency  $\Omega$  of 71.2 rad/s. In Fig. 10, the dot-and-dash line represents the initial liquid height (Eq. (7)) and the solid and the dash line show the wave pattern of the hydrostatic free-surface model and the SWE model at 0.05 s, respectively. The velocity vector field is naturally an output of the hydrostatic free-surface model. Both wave patterns are in a good agreement, despite a little phase error caused by the complete friction matrix used in the hydrostatic free-surface model.

## 5 Conclusions and Future Prospects

A shallow water model (SWE) for the flow of liquid metal layer on the inside surface of a rotating cylinder was developed. The objective was to study wave patterns of the free surface, wave birth, propagation, and death. Besides, the aim was also to study a response of the system on different initial conditions, i.e., the initial liquid height was either constant or perturbed using a sinelike function. The main assumptions of the model are: The angular frequency  $\Omega$  of the mold is so high that the fluid is mainly rotating with the cylinder. For this reason, the model was defined in the rotating frame of reference. A parabolic velocity profile along the liquid height was taken into account with a no-slip boundary condition on the cylindrical wall. The model was further extended in order to account for vibrations and an axis bending. The origin of the vibrations and the axis bending was explained by means of the natural frequencies and the corresponding mode shapes. It was shown that despite extremely high centrifugal forces ( $\sim 100$  G) acting on a liquid layer, the interaction between the inertia, the gravity, and the vibrations can lead to the formation of waves on the free surface. The higher the liquid height, the more it is prone to instabilities. The SWE model was successfully validated against a more complex, well-established hydrostatic free-surface model using a wave propagation test. In the future, a solidification model will be included using two layers approach, one for the liquid and one for the solidified layer by taking into account the heat conduction inside the mold and also heat losses into the ambient air. The magnitude of accelerations and flow velocities predicted by the present model leads to the idea that strong fragmentation of the solidified elements occurs. In order to take into account this phenomenon, a three-layer model will be under consideration.

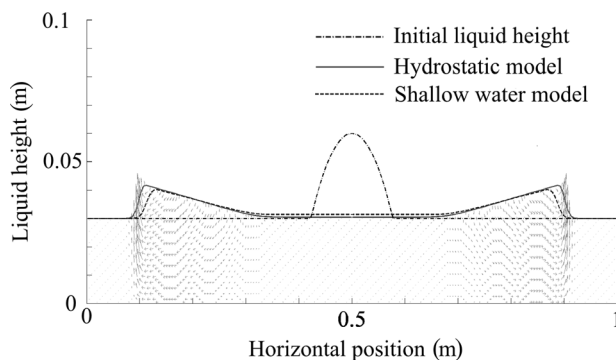


Fig. 11 Schematic of vectors

## Acknowledgment

Financial support by the Austrian Federal Government (in particular from the Bundesministerium für Verkehr, Innovation und Technologie and the Bundesministerium für Wirtschaft, Familie und Jugend) and the Styrian Provincial Government, represented by Österreichische Forschungsförderungsgesellschaft mbH and by Steirische Wirtschaftsförderungsgesellschaft mbH, within the research activities of the K2 Competence Centre on “Integrated Research in Materials, Processing and Product Engineering,” operated by the Materials Center Leoben Forschung GmbH in the framework of the Austrian COMET Competence Centre Programme, is gratefully acknowledged. This work was also financially supported by the Eisenwerk Sulzau-Werfen, R. & E. Weinberger AG.

## Appendix A: Bending of Mold Axis

Since the SWE are solved in the rotating frame of reference, it is convenient to introduce a global coordinate system  $C_G(\mathbf{x}', \mathbf{y}', \mathbf{z}')$  rotating with the angular velocity of the mold  $\Omega$ . A deformation of the mold axis (bending) is given by the following trigonometric function with nodes exactly positioned in the carrying rollers:

$$B = -A \cos\left(\frac{\pi x'}{\lambda}\right) \quad (A1)$$

where  $\lambda$  is the distance between the two coaxial rollers,  $A$  is the maximum amplitude of the bending (in the simulations  $A = 2$  mm), and  $B$  is the local amplitude, which is zero in the nodes, negative toward the mold center, and positive toward extremities (Fig. 11). The  $x'$  coordinate is zero at the center of the mold. The tangent  $\mathbf{c}$  of the deformed axis is defined by the slope of the  $B$ , which is given by

$$\begin{aligned} \tan \theta &= \frac{\partial B}{\partial x'} \\ &= A \frac{\pi}{\lambda} \sin\left(\frac{\pi x'}{\lambda}\right) \end{aligned} \quad (A2)$$

The tangent  $\mathbf{c}$  is then defined as

$$\mathbf{c} = \begin{bmatrix} 1 \\ \tan \theta \\ 0 \end{bmatrix} \quad (A3)$$

and denotes the axial direction. Similarly, in the radial direction we can define vector  $\mathbf{r}$  pointing outward from the  $x'$  axis

$$\mathbf{r} = \begin{bmatrix} R \sin \theta \cos \alpha \\ -R \cos \theta \cos \alpha \\ -R \sin \alpha \end{bmatrix} \quad (A4)$$

where  $R$  is the inner radius of the mold, and the angle  $\alpha$  defines the tangential position in radians around the circumference as follows:

$$\alpha = \frac{y}{R} \quad (A5)$$

where  $y$  is the circumferential position in meters. Finally, the cross product  $\mathbf{c} \times \mathbf{r}$  gives a vector  $\mathbf{d}$  representing the tangential direction

$$\mathbf{d} = \mathbf{c} \times \mathbf{r} = \begin{bmatrix} -R \sin \alpha \tan \theta \\ R \sin \alpha \\ -R(\cos \theta \cos \alpha + \sin \theta \cos \alpha \tan \theta) \end{bmatrix} \quad (A6)$$

The vectors  $\mathbf{c}$ ,  $\mathbf{d}$ , and  $\mathbf{r}$  are normalized.

## Appendix B: Centrifugal Force

In order to determine the centrifugal acceleration  $\mathbf{a}_c$  for each point inside the mold, we need to determine its distance from the  $x$ -axis in vectorial form. Let us call this vector as  $\mathbf{r}^*$ . The vector  $\mathbf{r}^*$  is defined as follows:

$$\mathbf{r}^* = \begin{bmatrix} 0 \\ B - R \cos \theta \cos \alpha \\ -R \sin \alpha \end{bmatrix} \quad (\text{B1})$$

The vector  $\mathbf{r}^*$  has the same orientation as the vector  $\mathbf{r}$ , i.e., from the mold center outward. The centrifugal acceleration  $\mathbf{a}_c$  is fully defined by the angular velocity  $\Omega$  and the vector  $\mathbf{r}^*$  by the formula

$$\mathbf{a}_c = \Omega \times (\Omega \times \mathbf{r}^*) \quad (\text{B2})$$

where  $\Omega$  is a vector with nonzero component only in  $x$ -direction.

$$\Omega = \begin{bmatrix} |\Omega| \\ 0 \\ 0 \end{bmatrix} \quad (\text{B3})$$

The resulting centrifugal acceleration  $\mathbf{a}_c$  points radially outward from the mold axis and is defined as follows:

$$\mathbf{a}_c = \begin{bmatrix} 0 \\ \Omega^2 (B - R \cos \theta \cos \alpha) \\ -\Omega^2 R \sin \alpha \end{bmatrix} \quad (\text{B4})$$

The centrifugal acceleration  $\mathbf{a}_c$  defined in this way cannot be, however, directly applied in the SWE model. The vector  $\mathbf{a}_c$  has to be transformed into the local coordinate system given by vectors  $\mathbf{c}$ ,  $\mathbf{r}$ , and  $\mathbf{d}$  denoting the axial, radial, and tangential direction, respectively (Appendix A). The axial component  $a_{ca}$  of centrifugal acceleration  $\mathbf{a}_c$  is obtained by projecting it into the axial direction given by vector  $\mathbf{c}$ , which is done simply by applying dot product as follows:

$$a_{ca} = \mathbf{a}_c \cdot \mathbf{c} \quad (\text{B5})$$

Similarly, the tangential  $a_{ct}$  and the radial  $a_{cr}$  components of centrifugal acceleration  $\mathbf{a}_c$  are derived as follows:

$$a_{ct} = \mathbf{a}_c \cdot \mathbf{d} \quad (\text{B6})$$

and

$$a_{cr} = \mathbf{a}_c \cdot \mathbf{r} \quad (\text{B7})$$

respectively. After evaluating the dot product of  $\mathbf{a}_c$  and  $\mathbf{r}$ , the radial component  $a_{cr}$  of the centrifugal acceleration  $\mathbf{a}_c$  finally becomes:

$$a_{cr} = \Omega^2 (R \sin^2 \alpha - \cos \theta \cos \alpha (B - R \cos \theta \cos \alpha)) \quad (\text{B8})$$

Note that  $a_{cr}$  stands for the radial component of the centrifugal acceleration  $\mathbf{a}_c$  but only at the inner mold surface. In order to calculate  $a_{cr}(z)$  as a function of radial distance  $z$  from the wall,  $R$  has to be replaced by  $R - z$ . Then, Eq. (B8) becomes

$$a_{cr}(z) = \Omega^2 (R - z) \sin^2 \alpha - \Omega^2 \cos \theta \cos \alpha (B - (R - z) \cos \theta \cos \alpha) \quad (\text{B9})$$

Since the flow (continuity and momentum equations) is solved using the SWE,  $a_{cr}$  from Eq. (B9) has to be first expressed as a hydrostatic pressure  $p_h$ . At an arbitrary point  $z_0$  within the liquid layer, the hydrostatic pressure  $p_h(z_0)$  is defined by the following formula:

$$p_h(z_0) = -\rho \int_{h+\delta}^{z_0} a_{cr}(z) dz \quad (\text{B10})$$

where  $h$  and  $\delta$  denote the height of liquid metal and the height of solid metal, respectively. Integration of Eq. (B10) results in rather lengthy formula and is not mentioned here. For the special case, when there is no axis deformation ( $B=0$  and  $\theta=0$ ), the hydrostatic pressure  $p_h$  at  $z_0$  reduces to

$$p_h(z_0) = -\frac{1}{2} \rho \Omega^2 (z_0 - h - \delta)(2R - z_0 - h - \delta) \quad (\text{B11})$$

Replacing  $z_0$  with  $z$  in Eq. (B10) and integrating the gradient of the hydrostatic pressure  $p_h(z)$  over the liquid height  $h$  gives us the force  $\mathbf{F}_c$  with the axial and tangential component, which then can be applied as source terms in momentum equations. This force  $\mathbf{F}_c$  is given by

$$\mathbf{F}_c = - \int_{\delta}^{h+\delta} \nabla p_h(z) dz \quad (\text{B12})$$

where  $\nabla p_h(z)$  is the gradient of hydrostatic pressure  $p_h(z)$ .  $\nabla p_h(z)$  has two components, axial and tangential. (The same procedure is also applied to other forces having a nonzero component in the radial direction  $z$ .) Let us first analyze the axial component of the force  $\mathbf{F}_c$  and let us again start with the special case, when there is no axis deformation ( $B=0$  and  $\theta=0$ ). (We suppress the subscripts  $c$  here and below for clarity, since we need to add other subscripts.) In this special case, the axial component of the force  $\mathbf{F}$  is simplified to

$$F_{rx} = -\rho \Omega^2 h (R - h - \delta) \frac{\partial(h + \delta)}{\partial x} \quad (\text{B13})$$

The tangential component  $F_{ry}$  is the same except that  $x$  is replaced by  $y$

$$F_{ry} = -\rho \Omega^2 h (R - h - \delta) \frac{\partial(h + \delta)}{\partial y} \quad (\text{B14})$$

In the general case, when the axis is deformed ( $B \neq 0$  and  $\theta \neq 0$ ), the formula for the force  $\mathbf{F}$  gets inconveniently long; nevertheless, for the sake of completeness it is given below. We again start with the force component  $F_{rx}$  exploded into several terms

$$\begin{aligned} F_{rx} = & \rho \Omega^2 ((Bbc - b^2 c^2 R - a^2 R) \left( h \frac{\partial(h + \delta)}{\partial x} \right) \\ & + (a^2 + b^2 c^2) \left( h^2 \frac{\partial(h + \delta)}{\partial x} \right) \\ & + (a^2 + b^2 c^2) \left( \delta h \frac{\partial(h + \delta)}{\partial x} \right) \\ & + \frac{1}{2} \frac{\partial B}{\partial x} bc (h^2) \\ & + \frac{1}{6} \frac{\partial c}{\partial x} (3Bb - 6b^2 c R) (h^2) \\ & + \frac{1}{6} \frac{\partial c}{\partial x} 4b^2 c (h^3) \\ & + \frac{1}{6} \frac{\partial c}{\partial x} 6b^2 c (\delta h^2) \end{aligned} \quad (\text{B15})$$

where  $a$ ,  $b$ , and  $c$  are substitutions for  $\sin \alpha$ ,  $\cos \alpha$ , and  $\cos \theta$ , respectively. These substitutions are also used in the definition of the force component  $F_{ry}$ , which is given by

$$\begin{aligned}
F_{ty} = & \rho\Omega^2((Bbc - b^2c^2R - a^2R)\left(h\frac{\partial(h+\delta)}{\partial y}\right) \\
& + (a^2 + b^2c^2)\left(h^2\frac{\partial(h+\delta)}{\partial y}\right) \\
& + (a^2 + b^2c^2)\left(\delta h\frac{\partial(h+\delta)}{\partial y}\right) \\
& - \frac{\partial a}{\partial y}aR(h^2) \\
& + \frac{2}{3}\frac{\partial a}{\partial y}a(h^3) \\
& + \frac{\partial a}{\partial y}a(\delta h^2) \\
& + \frac{1}{6}\frac{\partial b}{\partial y}(3Bc - 6bc^2R)(h^2) \\
& + \frac{1}{6}\frac{\partial b}{\partial y}4bc^2(h^3) \\
& + \frac{1}{6}\frac{\partial b}{\partial y}6bc^2(\delta h^2)
\end{aligned} \tag{B16}$$

Let us try to check the correctness of Eqs. (B15) and (B16) by setting  $B$  and  $\theta$  again equal to zero ( $c = \cos\theta = 1$ ), which means the mold axis is perfectly straight. Last four terms in Eq. (B15) cancel out and the equation reduces to Eq. (B13). Regarding Eq. (B16), last six terms also cancel out and the equation reduces to Eq. (B14).

To summarize, the radial component of centrifugal acceleration  $\mathbf{a}_c$  cannot be applied directly. It has to be expressed first as a hydrostatic pressure, then gradient of this pressure has to be calculated in tangential and axial direction. Finally, both components of pressure gradient have to be integrated over the liquid height  $h$ . The corresponding results then represent momentum source terms due to the radial component of centrifugal acceleration  $\mathbf{a}_c$ .

In addition to the radial component, the centrifugal acceleration  $\mathbf{a}_c$  can generally have also components in the tangential and the axial direction. The derivation of corresponding momentum sources is straightforward and easier than in the previous case of  $a_{cr}$ , since neither a computation of hydrostatic pressure nor its gradient is needed. The momentum source term for the axial direction resulting from the axial component of  $\mathbf{a}_c$  takes the following form:

$$F_{ax} = \int_{\delta}^{h+\delta} \rho a_{ca} dz \tag{B17}$$

where  $a_{ca}$  is the axial component of the centrifugal acceleration  $\mathbf{a}_c$ . Similarly, the momentum source term for the tangential direction resulting from the tangential component of  $\mathbf{a}_c$  is given by

$$F_{ty} = \int_{\delta}^{h+\delta} \rho a_{ct} dz \tag{B18}$$

After the integration of Eq. (B17),  $F_{ax}$  becomes

$$\begin{aligned}
F_{ax} = & \rho\Omega^2\frac{1}{|c|}((Be - bdeR)(h) \\
& + \frac{1}{2}(bde)(h^2) \\
& + (bde)(\delta h^2))
\end{aligned} \tag{B19}$$

where  $b$ ,  $d$ , and  $e$  are substitutions for  $\cos\alpha$ ,  $\cos\theta$ , and  $\tan\theta$ , respectively. For a mold without the axis bending  $\theta=0$ , then  $\tan\theta=0$  and thus,  $F_{ax}$  is zero. Similarly, after the integration of Eq. (B18),  $F_{ty}$  becomes

$$\begin{aligned}
F_{ty} = & \rho\Omega^2\frac{aR}{|d|}((B + befR)(h) \\
& - \frac{1}{2}(bef)(h^2) \\
& - (bef)(\delta h^2))
\end{aligned} \tag{B20}$$

where  $a$ ,  $b$ ,  $e$ , and  $f$  are substitutions for  $\sin\alpha$ ,  $\cos\alpha$ ,  $\tan\theta$ , and  $\sin\theta$ , respectively. In Eqs. (B19) and (B20),  $|c|$  and  $|d|$  correspond to vectors defined in Eqs. (A3) and (A6), respectively, i.e., those not normalized yet. Note again that for a mold without the axis bending  $\tan\theta=0$  and thus,  $F_{ty}$  is zero.

## Appendix C: Coriolis Force

The general vector formula for the Coriolis acceleration  $\mathbf{a}_c$  is

$$\mathbf{a}_c = -2\Omega \times \mathbf{u} \tag{C1}$$

where  $\Omega$  is the angular velocity described in Appendix B and  $\mathbf{u}$  is the relative velocity defined in the global coordinate system  $C_G(\mathbf{x}', \mathbf{y}', \mathbf{z}')$ . The components of the Coriolis acceleration  $\mathbf{a}_c$  in the global coordinate system  $C_G$  are

$$\mathbf{a}_c = \begin{bmatrix} 0 \\ a_{C_y'} \\ a_{C_z'} \end{bmatrix} \tag{C2}$$

The  $x$ -component  $a_{C_x'}$  is zero because the angular velocity  $\Omega$  is parallel to the  $x'$  axis. The relative velocity  $\mathbf{u}$  is computed in the local coordinate system  $C_L(\mathbf{c}, \mathbf{d}, \mathbf{r})$  with the following nonzero components:

$$\mathbf{v} = \begin{bmatrix} u_x \\ u_y \\ 0 \end{bmatrix} \tag{C3}$$

One of the assumptions of the SWE model is a negligible flux in the radial direction and thus, the radial component  $u_z$  of the relative velocity  $\mathbf{u}$  is zero. In order to transform the Coriolis acceleration  $\mathbf{a}_c$  into momentum source terms it is first projected onto the vectors  $\mathbf{c}$ ,  $\mathbf{d}$ , and  $\mathbf{r}$  as it was done for the centrifugal acceleration  $\mathbf{a}_c$  in Appendix B. After the projection the Coriolis acceleration  $\mathbf{a}_c$  in the local coordinate system,  $C_L$  becomes:

$$\mathbf{a}_c = \begin{bmatrix} a_{Ca} \\ a_{Ct} \\ a_{Cr} \end{bmatrix} = \begin{bmatrix} \mathbf{a}_c \cdot \mathbf{c} \\ \mathbf{a}_c \cdot \mathbf{d} \\ \mathbf{a}_c \cdot \mathbf{r} \end{bmatrix} \tag{C4}$$

First, the axial component  $a_{Ca}$  of the Coriolis acceleration  $\mathbf{a}_c$  is expressed as

$$\begin{aligned}
a_{Ca} = & 0c_{x'} + a_{C_y'}c_{y'} + a_{C_z'}0 \\
= & 2\Omega u_y c_{y'} d_{z'}
\end{aligned} \tag{C5}$$

after the substitution for  $c_{y'}$  and  $d_{z'}$  from Eqs. (A3) and (A6), respectively, Eq. (C5) would expand into an inconveniently long term; hence, it is not shown here. Similar relations can be found for the tangential  $a_{Cd}$  and the radial  $a_{Cr}$  components of the Coriolis acceleration  $\mathbf{a}_c$ , given by

$$\begin{aligned}
a_{Ct} = & 0d_{x'} + a_{C_y'}d_{y'} + a_{C_z'}d_{z'} \\
= & -2\Omega u_x c_{y'} d_{z'}
\end{aligned} \tag{C6}$$

and

$$\begin{aligned} a_{C_r} &= 0r_{x'} + a_{C_{y'}}r_{y'} + a_{C_{z'}}r_{z'} \\ &= 2\Omega(u_y d_z r_{y'} - u_x r_{z'} c_{y'} - u_y d_{y'} r_{z'}) \end{aligned} \quad (C7)$$

respectively. The axial  $u_x$  and the tangential  $u_y$  components (Eq. (C3)) of the relative velocity  $\mathbf{u}$  of the liquid are functions of the radial coordinate  $z$  and resemble the parabolic velocity profile with the no-slip BC on the mold wall (or the solid) and the zero stress on the free surface. The axial component  $u_x(z)$  can be expressed as a function of the radial coordinate  $z$  and the axial component of the mass averaged velocity  $\bar{u}_x$  as follows:

$$u_x(z) = -\frac{3\bar{u}_x(\delta - z)(\delta + 2h - z)}{2h^2} \quad (C8)$$

In a similar way, the tangential component  $u_y(z)$  can be written. Substituting  $u_y(z)$  into Eq. (C5) and applying the same integral as in Eq. (B17) lead to the momentum source term for the axial direction resulting from the axial component of the Coriolis acceleration  $\mathbf{a}_C$

$$F_{C_{ax}} = -2\rho\Omega bf\bar{u}_x h \quad (C9)$$

where  $b$  and  $f$  are  $\cos \alpha$  and  $\sin \theta$ , respectively. In the case without the axis bending,  $\sin \theta$  is zero and thus, the Coriolis force in the axial direction  $F_{C_{ax}}$  becomes zero. Comparing Eqs. (C5) and (C6) reveals that the momentum source term  $F_{C_{ty}}$  in the tangential direction resulting from the tangential component of the Coriolis acceleration  $\mathbf{a}_C$  is very much similar, given by

$$F_{C_{ty}} = 2\rho\Omega bf\bar{u}_x h \quad (C10)$$

Note again that without the axis bending ( $\sin \theta = 0$ ), the Coriolis force in the tangential direction  $F_{C_{ty}}$  also cancels out. In addition to  $F_{C_a}$  and  $F_{C_t}$ , the radial component  $F_{C_r}$  is derived following the same steps that were used for the derivation of the centrifugal force (Appendix B). Final formulas of both components,  $F_{C_{rx}}$  and  $F_{C_{ry}}$ , are

$$\begin{aligned} F_{C_{rx}} &= -\rho h \Omega \left( d \left( \frac{5}{2} \bar{u}_y \frac{\partial h}{\partial x} + 2\bar{u}_y \frac{\partial \delta}{\partial x} + \frac{5}{4} h \frac{\partial \bar{u}_y}{\partial x} \right) \right. \\ &\quad + af \left( \frac{5}{2} \bar{u}_x \frac{\partial h}{\partial x} + 2\bar{u}_x \frac{\partial \delta}{\partial x} + \frac{5}{4} h \frac{\partial \bar{u}_x}{\partial x} \right) \\ &\quad \left. + \frac{5}{4} (ad\bar{u}_x - f\bar{u}_y) h \frac{\partial \theta}{\partial x} \right) \end{aligned} \quad (C11)$$

and

$$\begin{aligned} F_{C_{ry}} &= -\rho h \Omega \left( d \left( \frac{5}{2} \bar{u}_y \frac{\partial h}{\partial y} + 2\bar{u}_y \frac{\partial \delta}{\partial y} + \frac{5}{4} h \frac{\partial \bar{u}_y}{\partial y} \right) \right. \\ &\quad \left. + af \left( \frac{5}{2} \bar{u}_x \frac{\partial h}{\partial y} + 2\bar{u}_x \frac{\partial \delta}{\partial y} + \frac{5}{4} h \frac{\partial \bar{u}_x}{\partial y} \right) + \frac{5}{4R} bf\bar{u}_x h \right) \end{aligned} \quad (C12)$$

respectively. The constants  $a$ ,  $b$ ,  $d$ , and  $f$  stand for  $\sin \alpha$ ,  $\cos \alpha$ ,  $\cos \theta$ , and  $\sin \theta$ . In the case without the axis bending, Eqs. (C11) and (C12) reduce to a simple formula, given by

$$F_{C_{rx,y}} = -\rho h \Omega \left( \frac{5}{2} \bar{u}_y \nabla h + 2\bar{u}_y \nabla \delta + \frac{5}{4} h \nabla \bar{u}_y \right) \quad (C13)$$

## Appendix D: Gravity Force

The acceleration of gravity  $\mathbf{a}_g$  is written in the global coordinate system  $C_G(\mathbf{x}', \mathbf{y}', \mathbf{z}')$  as follows:

$$\mathbf{a}_g = \begin{bmatrix} 0 \\ -g \cos(\Omega t) \\ g \sin(\Omega t) \end{bmatrix} \quad (D1)$$

where  $t$  is the time in seconds, and  $g$  is the magnitude of the gravitational acceleration. Note that the vector  $\mathbf{a}_g$  rotates against the angular velocity  $\Omega$  defined by Eq. (B3), which reflects the rotating frame of reference used. The initial position of the global coordinate system  $C_G$  with respect to the acceleration  $\mathbf{a}_g$  is fixed, since any possible phase shift  $\varphi_0$  might play a significant role only during the very first rotations of the mold. Momentum source terms are derived in the same way as those for the centrifugal force and the Coriolis force. After the projection of the vector  $\mathbf{a}_g$  onto the unit vector in the axial direction  $\mathbf{c}$ , the resulting axial component  $a_{g_a}$  multiplied by the liquid height  $h$  and density  $\rho$  leads to the following source term:

$$F_{g_{ax}} = -\rho h g f \cos(\Omega t) \quad (D2)$$

which becomes zero in the case without axis bending ( $f \cong \sin \theta = 0$ ). Similarly, the source term resulting from the tangential component  $a_{g_t}$  obtained by projecting it onto the unit vector  $\mathbf{d}$  is

$$F_{g_{ty}} = \rho h g (b \sin(\Omega t) + ad \cos(\Omega t)) \quad (D3)$$

When the axis bending is zero, after a few trigonometric operations it reduces to

$$F_{g_{ty}} = -\rho h g \sin(\Omega t + \alpha) \quad (D4)$$

Finally, the momentum source terms resulting from the radial component  $a_{g_r}$  are obtained by integrating the gradient of the hydrostatic pressure over the liquid height, multiplying it by the density  $\rho$ , and switching the sign. Both,  $F_{g_{rx}}$  and  $F_{g_{ry}}$  can be written as

$$\begin{aligned} F_{g_{rx}} &= -\rho h g \left( (bd \cos(\Omega t) - a \sin(\Omega t)) \frac{\partial(h + \delta)}{\partial x} \right. \\ &\quad \left. - \frac{1}{2} bf \cos(\Omega t) h \frac{\partial \theta}{\partial x} \right) \end{aligned} \quad (D5)$$

and

$$\begin{aligned} F_{g_{ry}} &= -\rho h g ((bd \cos(\Omega t) - a \sin(\Omega t)) \frac{\partial(h + \delta)}{\partial y} \\ &\quad - \frac{1}{2R} (ad \cos(\Omega t) + b \sin(\Omega t)) h) \end{aligned} \quad (D6)$$

respectively. Without the axis bending, Eq. (D5) reduces to

$$F_{g_{rx}} = -\rho h g \cos(\Omega t + \alpha) \frac{\partial(h + \delta)}{\partial x} \quad (D7)$$

whereas Eq. (D6) simplifies to

$$\begin{aligned} F_{g_{ry}} &= -\rho h g \cos(\Omega t + \alpha) \frac{\partial(h + \delta)}{\partial y} \\ &\quad + \rho \frac{h^2 g}{2R} \sin(\Omega t + \alpha) \end{aligned} \quad (D8)$$

## Appendix E: Gravity Force Perturbed Due to the Imperfect Roundness of the Mold

Vibrations induced in the horizontally rotating mold due to the noncircularity of the mold or the carrying rollers are taken into account by a time-dependent perturbation of gravity  $g(1 + \xi \cos(\omega t + \beta_0))$ , where  $\xi$  is a nonzero real number (in the simulations  $\xi = 2$ ),  $\omega$  is the angular frequency of the perturbation (in the simulations  $\omega = 2\Omega$ ), and  $\beta_0$  is the phase (in the simulations  $\beta_0 = \pi/2$ ). Labeling the perturbed gravity as  $g_p$ , the acceleration of the perturbed gravity  $\mathbf{a}_{gp}$  in the global coordinate system  $C_G(\mathbf{x}', \mathbf{y}', \mathbf{z}')$  can be expressed as

$$\mathbf{a}_{gp} = \begin{bmatrix} 0 \\ -g_p \cos(\Omega t) \\ g_p \sin(\Omega t) \end{bmatrix} \quad (\text{E1})$$

Comparing Eq. (D1) and Eq. (E1) leads to the conclusion that exactly the same formulas as derived in Appendix D can be used to determine components of the gravity force perturbed due to the imperfect roundness of the mold provided that  $g$  in Eqs. (D2)–(D7) is replaced by  $g_p$ .

## Appendix F: Bed Shear Force

The viscous term in Eq. (2) does not account for the shear force with the mold (or the solidified metal shell) following from the assumption of the parabolic velocity profile. The bed shear force can be, however, easily derived from the 3D stress tensor  $\tau$  and applied as an additional source term in both the axial and tangential direction. The stress tensor  $\tau$  can be expressed as a function of the symmetric part of the velocity gradient tensor as follows:

$$\tau = -\mu(\nabla \mathbf{u} + \nabla \mathbf{u}^T) \quad (\text{F1})$$

which is in exploded form given by

$$\tau = -\mu \begin{bmatrix} 2 \frac{\partial u_x}{\partial x} & \frac{\partial u_y}{\partial x} + \frac{\partial u_x}{\partial y} & \frac{\partial u_z}{\partial x} + \frac{\partial u_x}{\partial z} \\ \frac{\partial u_x}{\partial y} + \frac{\partial u_y}{\partial x} & 2 \frac{\partial u_y}{\partial y} & \frac{\partial u_z}{\partial y} + \frac{\partial u_y}{\partial z} \\ \frac{\partial u_x}{\partial z} + \frac{\partial u_z}{\partial x} & \frac{\partial u_y}{\partial z} + \frac{\partial u_z}{\partial y} & 2 \frac{\partial u_z}{\partial z} \end{bmatrix} \quad (\text{F2})$$

Generally, in momentum equations the viscous acceleration  $\mathbf{a}_\tau$  is expressed as a divergence of the stress tensor  $\tau$  divided by the density  $\rho$ , which for the incompressible flow results in

$$\begin{aligned} \mathbf{a}_\tau &= \nu \nabla^2 \mathbf{u} \\ &= \nu \left( \frac{\partial^2 \mathbf{u}}{\partial x^2} + \frac{\partial^2 \mathbf{u}}{\partial y^2} + \frac{\partial^2 \mathbf{u}}{\partial z^2} \right) \end{aligned} \quad (\text{F3})$$

In Eq. (E3), the last term  $\nu \partial^2 \mathbf{u} / \partial z^2$  is the missing part in the viscous term in Eq. (2) representing components of a shear force acting on a  $z$ -plane parallel to the axial and tangential direction, respectively. In order to apply such a force in the SWE, we have to first substitute for the velocity  $\mathbf{u}$  from Eq. (C8) and integrate it over the liquid height  $h$ . This leads to the final components  $F_{\tau a}$  and  $F_{\tau t}$  of the bed shear force in the axial and tangential direction

$$F_{\tau a} = -3\nu \frac{\bar{u}_x}{h} \quad (\text{F4})$$

and

$$F_{\tau t} = -3\nu \frac{\bar{u}_y}{h} \quad (\text{F5})$$

respectively.

## References

- [1] Shailesh, P., Kumar, B. P., Sundararajan, S., and Komariahia, M., 2012, "Experimental Investigation on Centrifugal Casting of 5500 Alloy: A Taguchi Approach," *Sci. Res. Essays*, **7**(44), pp. 3797–3808.
- [2] Chirita, G., Stefanescu, I., Barbosa, J., Puga, H., Soares, D., and Silva, F. S., 2009, "On Assessment of Processing Variables in Vertical Centrifugal Casting Technique," *Int. J. Cast Met. Res.*, **22**(5), pp. 382–389.
- [3] Chirita, G., Stefanescu, I., Soares, D., and Silva, F. S., 2006, "Centrifugal Versus Gravity Casting Techniques Over Mechanical Properties," *An. Mec. Fractura*, **1**, pp. 317–322.
- [4] Chang, S. R., Kim, J. M., and Hong, C. P., 2001, "Numerical Simulation of Microstructure Evolution of Al Alloys in Centrifugal Casting," *ISIJ Int.*, **41**(7), pp. 738–747.
- [5] Hirt, C. W., and Nichols, B. D., 1981, "Volume of Fluid (VOF) Method for the Dynamics of Free Boundaries," *J. Computat. Phys.*, **39**(1), pp. 201–225.
- [6] Keerthiprasad, K. S., Murali, M. S., Mukunda, P. G., and Majumdar, S., 2010, "Numerical Simulation and Cold Modeling Experiments on Centrifugal Casting," *Metall. Mater. Trans. B*, **42**(1), pp. 144–155.
- [7] Zagorski, R., and Sleziona, J., 2007, "Pouring Mold During Centrifugal Casting Process," *Arch. Mater. Sci. Eng.*, **28**(7), pp. 441–444.
- [8] Kaschnitz, E., 2012, "Numerical Simulation of Centrifugal Casting of Pipes," *IOP Conf. Ser.: Mater. Sci. Eng.*, **33**(1), p. 012031.
- [9] Daming, X., Limin, J., and Hengzhi, F., 2008, "Effects of Centrifugal and Coriolis Forces on the Mold-Filling Behavior of Titanium Melts in Vertically Rotating Molds," *China Foundry*, **5**(4), pp. 249–257.
- [10] Xu, Z., Song, N., Tol, R. V., Luan, Y., and Li, D., 2012, "Modelling of Horizontal Centrifugal Casting of Work Roll," *IOP Conf. Ser.: Mater. Sci. Eng.*, **33**(1), p. 012030.
- [11] Fjeld, A., and Ludwig, A., 2009, "Flow Patterns and Re-Melting During the Filling of a Large Composite Casting," *Int. J. Cast Met. Res.*, **22**(1–4), pp. 111–114.
- [12] Ludwig, A., Kharicha, A., and Wu, M., 2014, "Modeling of Multiscale and Multiphase Phenomena in Materials Processing," *Metall. Mater. Trans. B*, **45**(1), pp. 36–43.
- [13] Leveque, R. J., 2002, *Finite Volume Methods for Hyperbolic Systems*, Cambridge University Press, New York.
- [14] Dellar, P. J., and Salmon, R., 2005, "Shallow Water Equations With a Complete Coriolis Force and Topography," *Phys. Fluids*, **17**(10), pp. 1–23.
- [15] Hirt, C. W., and Richardson, J. E., 1999, "The Modeling of Shallow Flows," *Flow Sci. Tech. Notes*, **48**, pp. 1–14.
- [16] Lanser, D., Blom, J. G., and Verwer, J. G., 2001, "Time Integration of the Shallow Water Equations in Spherical Geometry," *Modell. Anal. Simul.*, **17**(1), pp. 373–393.
- [17] Audusse, E., Bouchut, F., Bristeau, M.-O., Klein, R., and Perthame, B., 2004, "A Fast and Stable Well-Balanced Scheme With Hydrostatic Reconstruction for Shallow Water Flows," *SIAM J. Sci. Comput.*, **25**(6), pp. 2050–2065.
- [18] Martinez, G., Garnier, M., and Durand, F., 1987, "Stirring Phenomena in Centrifugal Casting of Pipes," *Appl. Sci. Res.*, **44**(1–2), pp. 225–239.
- [19] Love, A. E. H., 1888, "The Small Free Vibrations and Deformations of a Thin Elastic Shell," *Philos. Transl. R. Soc. London, Ser. A*, **179**, pp. 491–546.
- [20] Donnell, L. H., 1935, "Stability of Thin-Walled Tubes Under Torsion," *N.A.C.A. Report No. 479*.
- [21] Li, H., Lam, K.-Y., and Ng, T.-Y., 2005, *Rotating Shell Dynamics*, Elsevier, London.
- [22] Bryan, G. H., 1890, "On the Beats in the Vibration of Revolving Cylinder or Bell," *Proc. Cambridge Philos. Soc.*, **7**(3), pp. 101–111.
- [23] Casulli, V., 1999, "A Semi-Implicit Finite Difference Method for Non-Hydrostatic, Free-Surface Flows," *Int. J. Numer. Methods Fluids*, **30**(4), pp. 425–440.
- [24] Osher, S., and Sethian, J. A., 1988, "Fronts Propagating With Curvature-Dependent Speed: Algorithms Based on Hamilton-Jacobi Formulations," *J. Comput. Phys.*, **79**(1), pp. 12–49.